

<https://doi.org/10.1038/s41538-026-00714-w>

Structural divergence of *Lentinula edodes* polysaccharides is associated with distinct anti-hyperuricemia pathways

Check for updates

Xinyi Xiong^{1,2}, Peng Liu¹, Liping Liu¹, Jie Feng¹, Jingsong Zhang¹, Jinyan Wang¹, Jie Geng¹ & Yanfang Liu¹ ✉

Lentinula edodes (*L. edodes*) polysaccharides hold therapeutic potential for hyperuricemia (HUA), but their mechanisms remain unclear. This study investigated the anti-HUA effects and associated regulatory pathways of two structurally distinct polysaccharides (LEP20 and LEP50) from *L. edodes*. Structural analysis identified LEP20 as a (1 → 3)- β -D-glucan (M_w , 1.96×10^6 g/mol) and LEP50 as a (1 → 4)- α -D-glucan (M_w , 1.46×10^7 g/mol). In a HUA rat model, both LEP20 and LEP50 significantly reduced serum UA level, inhibited xanthine oxidase, and alleviated renal injury and inflammation. Mechanistically, LEP20 was linked to modulate the gut-kidney axis by regulating UA transporters, enriching beneficial gut microbiota (e.g., *Blautia_luti*), and promoting short-chain fatty acid production to restore intestinal barrier integrity. In contrast, LEP50 primarily regulated systemic purine metabolism, directly reducing hypoxanthine levels and modulating specific gut microbes (e.g., *Romboutsia_ilealis*). The distinct structural features of these polysaccharides are associated with different regulatory pathways, supporting their potential application in HUA management.

Hyperuricemia (HUA) is a metabolic disorder characterized by elevated serum uric acid (UA) levels, which has emerged as a significant global health burden¹. The global prevalence of HUA and gout rose to 55.8 million cases in 2020, marking a 22.5% increase over the three decades since 1990². Chronic UA overload not only drives gout and nephrolithiasis but also exacerbates systemic inflammation and multi-organ dysfunction, particularly renal tubular injury and hepatic metabolic dysregulation³. The xanthine oxidase (XOD) inhibitors and UA transporter 1 (URAT1) blockers are currently commonly used in the treatment of HUA⁴. These pharmacotherapies are effective in UA reduction, but their long-term use is limited by adverse reactions, such as severe cutaneous toxicity, hepatotoxicity, and increased cardiovascular risk. For example, allopurinol has been associated with severe skin adverse reactions, and febuxostat with increased risk of cardiovascular death⁵. Moreover, these drugs primarily target single enzymes or transporters, which may not sufficiently address the multifactorial pathological network of HUA involving oxidative stress, inflammation, renal dysfunction, and gut microbiota imbalance. Therefore, it is necessary to search for natural products to treat or relieve HUA, which possess high molecular diversity and novel bio-functionality, as well as superior safety profiles.

Natural polysaccharides constitute a class of natural macromolecules which have been shown to exhibit complex, important and multifaceted biological activities, including antitumor, antioxidative, antiviral, immunomodulatory activities⁶. Importantly, polysaccharides have demonstrated multi-target regulatory potential in multiple metabolic and inflammatory pathways relevant to HUA, suggesting that they might offer a multi-target, systems-level therapeutic advantage over conventional single-target drugs. Accumulating evidences indicated that polysaccharides derived from *Phellinus_ignarius*, *Ganoderma_lucidum* and corn silk^{7,8} exhibited certain inhibitory effects on UA production. Current research consensus demonstrate that the bioactivity of polysaccharides is closely linked to their structural features, with critical parameters, such as glycosidic linkage types in the backbone, degree of branching, and molecular weight profoundly influencing solubility, intestinal absorption, and binding capacity to targets⁹. However, their mechanisms of action are primarily studied within isolated pathways rather than in the context of integrated biological systems. Furthermore, the structure-activity relationships underlying these bioactive effects have yet to be systematically elucidated through integrated experimental approaches. For instance, β -(1 → 3)-D-glucans have demonstrated that they enhanced immune receptor binding affinity due to their distinctive helical conformation¹⁰, while α -linked isomers were more readily absorbed

¹Institute of Edible Fungi, Shanghai Academy of Agricultural Sciences; Key Laboratory of Edible Fungi Resources and Utilization (South), Ministry of Agriculture and Rural Affairs, P.R. China; National Engineering Research Center of Edible Fungi; National R&D Center for Edible Fungi Processing, Shanghai, China. ²State Key Laboratory of Food Science and Technology, China-Canada Joint Lab of Food Science and Technology (Nanchang), Nanchang University, 235 Nanjing East Road, Nanchang, Jiangxi, China. ✉e-mail: aliu-1980@163.com

through intestinal pathways or metabolized by gut microbiota to exert systemic regulatory effects¹¹. However, the relationship between the structural specificity and activity of polysaccharides has not been verified in the context of HUA. *Lentinula edodes* (*L. edodes*) polysaccharides have been proven to exhibit diverse pharmacological activities including immunomodulation, antioxidant effects, antitumor properties and metabolic regulation¹², which suggested that polysaccharides might constitute the core material basis for intervention of *L. edodes* in UA metabolism. Notably, our previous research found that the extract of *L. edodes*, mainly composed of polysaccharides, had unique effect in lowering UA levels, reflecting in regulating renal UA transporters, relieving oxidative stress and inflammation, as well as modifying gut microbiota dysbiosis¹³, highlighting the potential of *L. edodes* polysaccharides as safer, multi-target natural agents for HUA management. However, the specific active polysaccharide components contributing to these effects remain unresolved, emphasizing the need to identify the key bioactive constituents and clarify their mechanistic roles.

Herein, we hypothesized that structural differences between LEP20 and LEP50 drive divergent anti-HUA mechanisms via organ-microbiota-metabolite interactions. Our study innovatively addressed these gaps by isolating two homogeneous polysaccharides from *L. edodes* (LEP20 and LEP50) with different structural characteristic. And the differences in HUA-alleviating potency of LEP20 and LEP50 was systematically evaluated using a multi-organ assessment framework spanning renal urate transporters, hepatic xanthine oxidase activity and intestinal barrier integrity in a potassium oxonate (PO)- and hypoxanthine-induced HUA rat model. Furthermore, an integrated microbiomes and metabolomics approach was employed to decipher the gut-mediated regulatory network. This study described associations between polysaccharide structural features and their divergent effects related to HUA improvement, which provides theoretical support for the precise utilization of *L. edodes* polysaccharide and the development of functional products for improving HUA.

Results and Discussion

Physical and chemical properties of LEP20 and LEP50

In this study, purified *L. edodes* polysaccharides (LEP) fractions coded as LEP20 and LEP50 were obtained by ethanol precipitation (Fig. 1A), a method that selectively precipitates polysaccharides based on their solubility in ethanol-water mixtures¹⁴. Higher ethanol concentrations typically favor the precipitation of polysaccharides with lower molecular weights, as observed in previous studies¹⁵. Based on the molecular weight distribution characters of polysaccharide fractions in water extract of *L. edodes*, stepwise precipitation with 20% and 50% of ethanol were performed to obtain LEP20 and LEP50, which exhibited yields of 1.40% and 1.24% (w/w) on the basis of the dry weight of fruit bodies, respectively. LEP20 contained 92.33% total sugar and 0.53% protein, while LEP50 contained 97.98% total sugar and 0.25% protein. Weight-average molecular weight (M_w) of LEP20 and LEP50 was 1.96×10^6 and 1.46×10^7 g/mol, respectively. The HPSEC chromatogram showed that LEP20 and LEP50 could be separated by fractional ethanol precipitation method (Fig. 1B). Moreover, both polysaccharides were homogeneous elution profiles, and polydispersity of them was close to 1.00, indicating that LEP20 and LEP50 were homogeneous polysaccharides. The monosaccharide composition analysis further showed that LEP20 and LEP50 were homoglucons (Fig. 1C). Although both LEP20 and LEP50 were identified as homoglucons, their distinct molecular weights and chromatographic behaviors suggested structural differences arising from variations in chain conformation, branching patterns, or glycosidic linkage types. LEP50 exhibited a later retention time than LEP20 in HPSEC analysis despite its higher molecular weight, suggesting that retention time was not solely governed by molecular weight but also influenced by other structural factors. The observation that a higher molecular weight polysaccharide eluted later might stem from molecular conformation-driven differences in hydrodynamic volume, the similar trend has been noted in *Rosa roxburghii* Tratt fruit polysaccharide extraction¹⁶. Linear or rigid glucans typically occupy a larger hydrodynamic volume and elute earlier, whereas branched or compact conformations reduce the effective size in solution, delaying

elution despite higher molecular weight¹⁷. Thus, LEP50's later retention time might reflect a more branched or tightly coiled structure compared to LEP20, which likely adopts a relatively linear or extended conformation. In summary, while LEP20 and LEP50 shared a glucan backbone, their divergent molecular weights and HPSEC profiles strongly suggested distinct architectures.

Methylation analysis of LEP20 and LEP50

Comparative methylation profiling of LEP20 and LEP50 revealed distinct glucan architectures, as illustrated in Fig. 1D, E and Table 1. LEP20 featured a (1 → 3)-D-glucan backbone with O-6 branching, (1 → 3)-linkages and branched units in a molar ratio of 1.06:1.76:1.00 (Fig. 1D). This corresponds to 1 branch per 2.5 backbone units. In contrast, LEP50 adopted a predominantly linear (1 → 4)-D-glucan structure containing terminal Glcp-(1 → residues, (1 → 4)-linkages, and (1 → 4,6)-branched points at a molar ratio of 1.30:6.62:1.00 (Fig. 1E), indicating significantly sparser O-6 branching with only one branch per eight backbone units. These findings demonstrated that LEP20 consists of a (1 → 3)-Glcp main chain with a terminal Glcp as the side chain at O-6, while LEP50 represents an O-6-branched (1 → 4)-D-glucan.

NMR analysis of LEP20 and LEP50

The primary structure of LEP20 and LEP50 were further confirmed by NMR spectroscopy and signals were assigned using 1D (¹H and ¹³C) and 2D (COZY, TOCSY, HMBC, HMQC and NOESY) NMR spectra. The elucidation of sugar residues was performed by comparing the chemical shifts of signals to the related values in the literature.

The β-configuration of glucose residues in LEP20 was confirmed by anomeric proton signals at δ 4.22 and 4.52 in the ¹H NMR anomeric region (Fig. 2A), with an integrated peak area ratio of 5:2 consistent with methylation analysis. Complementary evidence emerged from the ¹³C NMR spectrum (Fig. 2B), where anomeric carbons at δ 103.3 and 103.4 reinforced the β-configuration. A characteristic downfield signal at δ 86.4 indicated C-3 substitution. Through integrated analysis of anomeric proton chemical shifts and methylation data, specific assignments were established with δ 4.53/4.52 corresponding to →3)-Glcp-(1 → and →3,6)-Glcp-(1 → H-1 protons, while δ 4.22 was attributed to Glcp-(1 → . These residues were systematically designated A, B, and C based on anomeric proton downfield order.

Residue A: The H-1 signal at δ 4.53 exhibited COZY correlations to H-2 (δ 3.33) as shown in Fig. 2C, with subsequent TOCSY-driven assignments in Fig. 2D revealing sequential proton resonances from H-3 (δ 3.46) through H-6. All ¹H/¹³C correlations mapped via HSQC analysis (Fig. 2E, Table 2) were anchored by the diagnostic C-3 signal at δ 86.9, conclusively identifying the residue as →3)-β-D-Glcp-(1 → .

Residue B: Exhibiting H-1 at δ 4.52, COZY/TOCSY correlations established H-2 to H-6 assignments. HSQC-derived ¹³C shifts (Table 2) revealed dual substitution through downfield C-3 (δ 86.1) and C-6 (δ 68.6), characteristic of →3,6)-β-D-Glcp-(1 → .

Residue C: According to the H-1/C-1 (δ 4.22/103.4) of sugar residue C in Table 2, which was presumed to be a β-configuration glucose residue. COZY/TOCSY correlations confirmed H-2 to H-6 assignments, with HSQC validation (Fig. 2E) confirming its terminal structure as β-D-Glcp-(1 → .

The connectivity sequence among the three sugar residues was determined through HMBC and NOESY analyses (Fig. 2F, G and Table S2). The HMBC spectrum (Fig. 2F) revealed cross-peaks between H-1 (δ 4.53) of Residue A and C-3 (δ 86.1) of Residue B. Reciprocal correlations were observed between H-1 (δ 4.52) of Residue B / C-3 (δ 86.9) of Residue A, confirming the A-B linkage. Additionally, a cross-peak connecting H-1 (δ 4.22) of Residue C to C-6 (δ 68.6) of Residue B established the B-C connectivity. NOESY (Fig. 2G) further validated these linkages. Spatial proximities between H-1 (δ 4.53) of Residue A and H-3 (δ 3.48) of Residue B corroborated the A-B interaction. Critical NOESY correlations at δ 4.22/4.05 (C-H1/B-H6a), δ 4.22/3.55 (C-H1/B-H6b), δ 4.52/3.68 (B-H1/C-H6a),

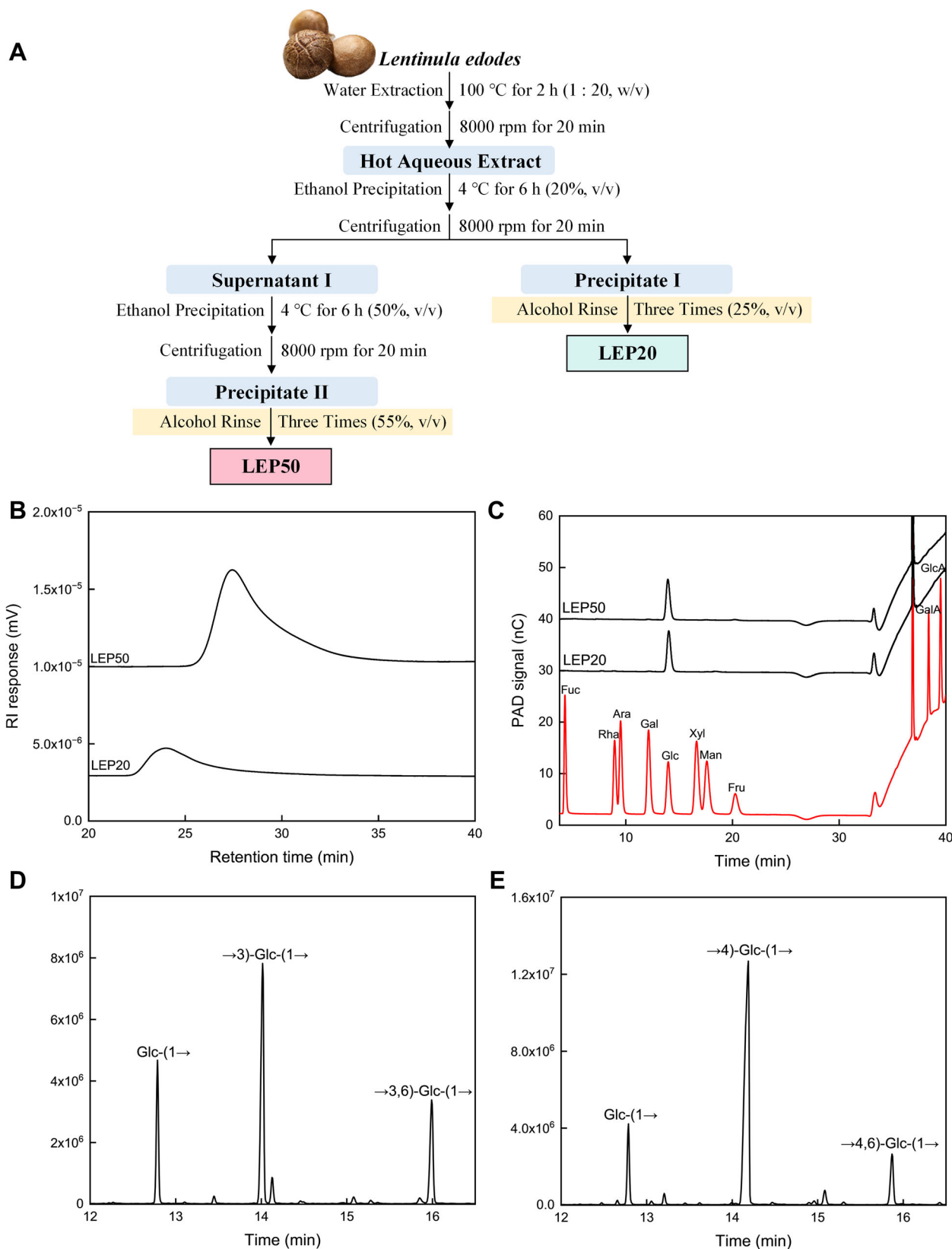


Fig. 1 | Preparation, compositional and macromolecular of LEP fractions. Preparation procedures of LEP fractions (A). HPSEC profiles (B), monosaccharide compositions (C), total ion chromatogram of the methylated products of LEP20 (D) and LEP50 (E).

and δ 4.52/3.45 (B-H1/C-H6b) provided conclusive evidence for the B-C linkage. The primary structure of LEP20 repeat unit was shown in Fig. 2H through the above results which featured a (1 → 3)- β -D-glucan backbone with two (1 → 6)- β -D-branch side-branching unit on every five backbone

units, the structure of LEP20 identified here was consistent with β -glucans extracted from *L. edodes* in previous study¹⁸.

The signal assignments for LEP50 were systematically established by integrating monosaccharide composition, glycosidic linkage patterns, and

Table 1 | Molar ratios analysis of linkage types of residues in LEP20 and LEP50 fractions

Linkage types	Molar ratios/%	
	LEP20	LEP50
Glc _p -(1→	27.65	14.57
→3)-Glc _p -(1→	46.18	-
→3,6)-Glc _p -(1→	26.17	-
→4)-Glc _p -(1→	-	74.22
→4,6)-Glc _p -(1→	-	11.21

chemical shift data. The ¹H NMR spectrum (Fig. 2I) exhibited two anomeric proton signals at δ 5.34 and δ 4.95 within the δ 4.95–5.34 region, displaying an integrated peak area ratio of 8:1. Methylation analysis revealed that δ 5.34 corresponds to two distinct residues, →4)-Glc_p-(1→ and →4,6)-Glc_p-(1→ (total 88.79% of glycosidic linkages), while δ 4.95 was assigned to Glc_p-(1→ (11.21%). Residues A, B and C were classified based on anomeric proton downfield order. The ¹³C NMR spectrum (Fig. 2J) showed two anomeric carbons at δ 100.50 and δ 78.70, collectively supporting an α-configuration with C-4 substitution across all residues. Sequential COZY correlations (Fig. 2K) for Residue A began at H-1 (δ 5.34), progressing to H-2 (δ 3.61) and H-3 (δ 3.82). TOCSY data (Fig. 2L) confirmed H-3 and H-4 assignments, while HSQC analysis (Fig. 2M) mapped all ¹H/¹³C correlations (Table 3). The diagnostic C-4 downfield shift (δ 78.2) confirmed Residue A as →4)-α-D-Glc_p-(1→. Similarly, Residue B was identified as →4,6)-α-D-Glc_p-(1→ through C-4 (δ 77.5) and C-6 (δ 69.7) substitutions, and Residue C as terminal α-D-Glc_p-(1→ via H-1/C-1 (δ 4.95/98.7) (Table 3).

HMBC correlations (Fig. 2N, Table S3) revealed bidirectional A-B connectivity through cross-peaks between H-1 (δ 5.34) of A / C-4 (δ 77.5) of B and H-1 (δ 5.34) of B / C-4 (δ 78.2) of A. NOESY data (Fig. 2O, Table S3) further confirmed spatial proximities between H-1 (δ 5.34) of A / H-4 (δ 3.63) of B and H-1 (δ 5.34) of B / H-4 (δ 3.60) of A, while cross-peaks at δ 5.34/3.95 (B-H1/C-H6a), δ 5.34/3.74 (B-H1/C-H6b), δ 4.94/3.42 (C-H1/B-H6a), and δ 4.94/3.93 (C-H1/B-H6b) established B-C linkages. Analysis of the aforementioned results revealed that the primary structural repeating unit of LEP50 comprises a backbone of α-(1→4)-D-Glc_p backbone and α-Glc_p branches at O-6, with a main chain-to-branch unit ratio of 8:1, as structurally depicted in Fig. 2P. The α-(1→4)-glucoside bond of LEP50 exhibited a structural unit less common in *L. edodes*, but observed in *Dicthyophora echinovolvata*¹⁹.

LEP20 and LEP50 reducing UA level and ameliorating renal injury

Elevated serum UA concentration is the hallmark diagnostic criterion for HUA, directly reflecting disrupted purine metabolism and impaired renal excretion²⁰. In this study, the MC group exhibited a significant increase in serum UA level compared to the NC group, confirming successful induction of HUA model. Both LEP fractions (LEP20 and LEP50) demonstrated potent UA-lowering effects, serum UA from 197.75 μmol/L to 89.89 and 105.80 μmol/L and the corresponding inhibition rates were 54.55% and 46.50%, respectively (Fig. 3A). This aligned with clinical observations that UA-lowering interventions were critical for mitigating HUA progression²¹. Consistent with our findings, bioactive polysaccharides from diverse natural sources exhibit UA-lowering properties. For instance, *Sphacelotheca reiliana* polysaccharides reduced serum UA by 27.91% in HUA rats through improvements of gut microbiota structure and metabolite profile²², while corn silk neutral polysaccharides achieved a 45.71% reduction via reduction of UA synthesis²³. Green alga *Enteromorpha prolifera* polysaccharides further demonstrated a UA decrease by modulating UA synthesis and excretion, and promoting gut microbiota-mediated UA degradation²⁴. Notably, LEP20 outperformed LEP50 in UA inhibition. While further structural validation is needed, this difference suggests a potential role for the specific triple helix configuration and receptor interactions often associated with β-glucans²⁵.

Sustained HUA induced renal dysfunction, as evidenced by elevated serum CRE and BUN, which served as key biomarkers for glomerular filtration rate decline and tubular injury²⁶. The serum CRE and BUN levels in the MC group were significantly higher than those in the NC group, indicating marked renal impairment in HUA rats (Fig. 3B and C). Treatment with LEP20 and LEP50 significantly attenuated these indicators, and compared to the model group, they respectively reduced serum CRE levels by 42.12% and 33.33%, as well as BUN levels by 42.12% and 33.33%, respectively, which indicated restored renal filtration capacity and tubular integrity. Chronic HUA triggered structural renal damage, including glomerular atrophy, tubular degeneration and renal fibrosis²⁷. Histopathological analysis (Fig. 3E) revealed intact renal structures in the NC group, characterized by uniform glomeruli, clear capillary loops, and well-organized tubular epithelial cells. In contrast, the MC group displayed severe renal damage, including glomerular atrophy, collapsed capillaries, thickened basement membranes, tubular dilation, vacuolization, and interstitial inflammatory infiltration. LEP20 and LEP50 interventions ameliorated these pathological changes, restoring glomerular space, reducing tubular vacuolization and dilation, and mitigating inflammatory cell infiltration. Masson staining (Fig. 3F) and collagen volume fraction analysis (Fig. 3D) demonstrated pronounced renal fibrosis in the MC group, with widened mesangial areas, increased matrix deposition, and extensive collagen fiber proliferation (blue staining). Both LEP20 and LEP50 treatments significantly alleviated fibrosis, as evidenced by reduced collagen accumulation and diminished blue-stained areas in renal tissues. In summary, LEP20 and LEP50 exerted ameliorative effects on renal function and histopathological damage in HUA rats, highlighting their potential as therapeutic agents for HUA-associated renal injury.

LEP20 and LEP50 suppressing renal inflammation and oxidative stress

The deposition of urate crystals in joints or tissues triggered their recognition and phagocytosis by macrophages via specific receptors, leading to increased infiltration of CD68-positive macrophages and subsequent release of pro-inflammatory cytokines (e.g., IL-1β, TNF-α, IL-6), and anti-inflammatory factors, such as IL-10 counteract these effects by polarizing macrophages toward an anti-inflammatory phenotype^{28,29}. This cascade exacerbated local inflammation and promoted the onset of gouty arthritis. To evaluate the anti-inflammatory effects of LEP20 and LEP50, the mRNA expression levels of pro-inflammatory cytokines (IL-1β, TNF-α, IL-6), anti-inflammatory cytokine IL-10 in the renal tissue of HUA rats were measured, and the level of CD68 was also determined by immunohistochemical staining method. As shown in Fig. 3G–J, renal mRNA levels of IL-1β, TNF-α, and IL-6 were significantly elevated in the MC group compared to the NC group, while IL-10 expression showed a downward trend in MC group. Following intervention with LEP20 and LEP50, these cytokines returned to normal, whereas LEP20 comparatively exhibited stronger anti-inflammatory efficacy compared to LEP50. Immunohistochemical analysis of CD68-positive macrophages (Fig. 3K) revealed dense infiltration and clustered aggregation around damaged renal tubules and vessels in the MC group versus NC group. LEP20 and LEP50 treatments markedly reduced CD68-positive cell counts compared to the MC group. Conclusively, LEP20 and LEP50 likely attenuated renal inflammation in HUA rats by suppressing CD68-positive macrophage infiltration and pro-inflammatory cytokine release. Notably, LEP20 showed superior efficacy in ameliorating renal inflammation, highlighting its therapeutic potential for HUA-associated pathologies. The superior anti-inflammatory efficacy of LEP20 over LEP50 is likely to be consistent with structural distinctions. Previous studies suggested that (1→3)-β-D-glucans, due to their triple helix conformation, were more readily recognized by immune cells to activate anti-inflammatory signaling pathways³⁰. In addition, β-glucans have been demonstrated to exert anti-inflammatory effects through multiple mechanisms, including inhibiting the production of inflammatory mediators, regulating NF-κB and MAPK signaling pathways³¹. In contrast, the anti-inflammatory potential

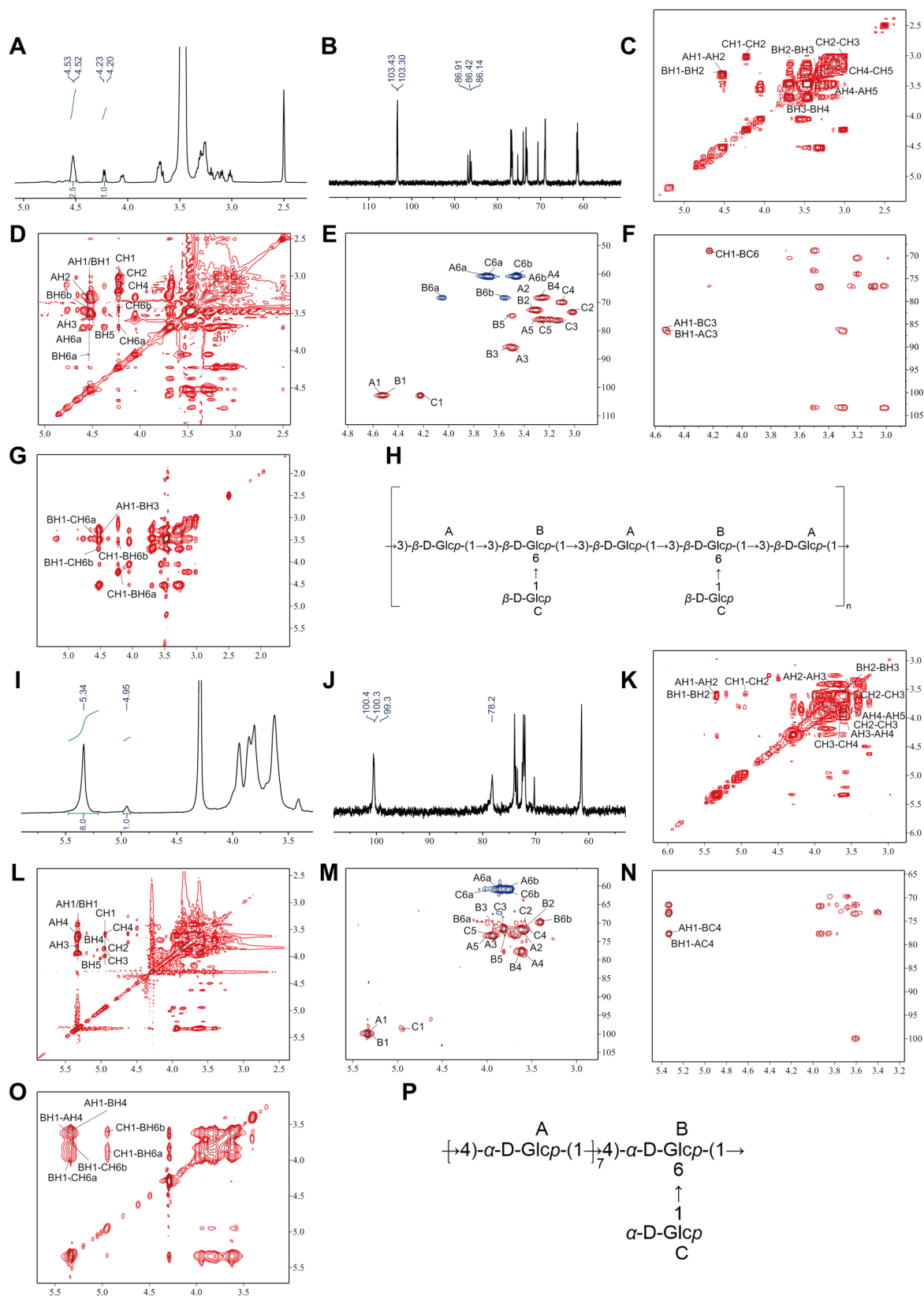


Fig. 2 | NMR spectra of LEP20 and LEP50. NMR spectra of LEP20 (A–G) and LEP50 (I–O) acquired at 70 °C, including ¹H NMR (A, I), ¹³C NMR (B, J), COZY (C, K), TOCSY (D, L), HSQC (E, M), HMBC (F, N), NOESY (G, O), and the structural repeating units of the LEP20 (H) and LEP50 (P).

of α -glucans remained largely unexplored with limited research reported in this area. This could explain why LEP20 exhibited superior efficacy in suppressing CD68 macrophage infiltration and pro-inflammatory cytokine expression.

Oxidative stress and inflammation are pathophysiologically intertwined in HUA progression, where reactive oxygen species (ROS) activate NLRP3 inflammasome pathways, amplifying pro-inflammatory cytokine production, such as IL-1 β and TNF- α ³². Conversely, antioxidant enzymes

Table 2 | Chemical shifts assignments from LEP20

Glycosyl residue	Chemical shifts / ppm						
	H1/C1	H2/C2	H3/C3	H4/C4	H5/C5	H6a/C6	H6b
→3)-β-D-Glcp-(1→	4.53	3.33	3.46	3.26	3.29	3.69	3.46
A	103.3	72.7	86.9	68.2	76.6	61.3	
→3,6)-β-D-Glcp-(1→	4.52	3.29	3.48	3.28	3.52	4.05	3.55
B	103.3	73.3	86.1	68.6	74.8	68.6	
β-D-Glcp-(1→	4.22	3.01	3.11	3.08	3.26	3.68	3.45
C	103.4	73.40	76.2	69.9	76.5	60.9	

Table 3 | Chemical shifts assignments from LEP50

Glycosyl residue	Chemical shifts / ppm						
	H1/C1	H2/C2	H3/C3	H4/C4	H5/C5	H6a/C6	H6b
→4)-α-D-Glcp-(1→	5.34	3.61	3.82	3.60	3.98	3.92	3.75
A	100.3	71.8	71.4	78.2	73.5	61.1	
→4,6)-α-D-Glcp-(1→	5.34	3.59	3.91	3.63	3.81	3.42	3.93
B	100.4	70.9	70.5	77.5	72.4	69.7	
α-D-Glcp-(1→	4.95	3.60	3.85	3.57	3.98	3.95	3.74
C	98.7	70.70	71.1	71.7	72.9	61.5	

like CAT and SOD neutralize ROS, thereby breaking this vicious cycle. Therefore, GSH concentration, CAT and SOD activities in renal tissues were measured to further investigate the effects of different LEP fractions on oxidative stress in HUA rats. Compared to the NC group, the MC group exhibited a significant decline in antioxidant capacity, with GSH concentration reduced by 20.15%, and CAT and SOD activities decreased by 31.95% and 9.59%, respectively (Fig. 3L–N). Notably, LEP20 and LEP50 interventions demonstrated differential regulatory effects on oxidative markers. CAT activity in the treated groups increased to 1.52- and 1.51-fold of the MC group, while GSH levels were elevated by 0.29- and 0.31-fold, respectively. SOD activity also improved, showing 0.27- and 0.23-fold increases compared to the MC group. Both LEP20 and LEP50 significantly enhanced renal antioxidant capacity, which aligned with established evidence that bioactive polysaccharides mitigate oxidative stress by scavenging free radicals and upregulating endogenous antioxidant defense systems³³. Notably, the significant enhancement of LEP20 activity against CAT might be related to the β-conformation, as β-glucans was hypothesized to stabilize antioxidant enzymes³⁴.

LEP20 and LEP50 modulating renal UA transporters

UA transporters in the kidney played a pivotal role in UA excretion and homeostasis. URAT1 and GLUT9 primarily mediated UA reabsorption, while ABCG2 and OAT1 were key secretory proteins responsible for UA excretion³⁵. To explore the regulatory effects of LEP20 and LEP50 on serum UA levels, the renal expression levels of these UA transporters (URAT1, GLUT9, ABCG2, and OAT1) in renal tissues were analyzed. As shown in Fig. 4A–D, the URAT1 and GLUT9 expressions of renal tissues in the MC group were upregulated, thereby impeding UA excretion. LEP20 and LEP50 respectively inhibited URAT1 expression by 44.37% and 20.76%, and suppressed GLUT9 levels by 34.59% and 21.01%. These results indicated that LEP fractions were associated with reduced reabsorption-related transporter expression to promote UA excretion, but LEP20 exhibited superior efficacy compared to LEP50. Conversely, the expressions of secretory transporters OAT1 and ABCG2 (Fig. 4E–H) were markedly

downregulated in the MC group versus the NC group. Interventions of LEP significantly restored OAT1 and ABCG2 expressions in a dose-dependent manner, among which LEP20 demonstrated a stronger regulatory effect compared to LEP50. LEP20 and LEP50 ameliorated HUA by engaging with dual modulation pathways of UA transporters, namely suppressing UA reabsorption and enhancing UA excretion. However, LEP20 displayed the more potent regulatory effects than LEP50. The modulation of UA transporters by LEP20 and LEP50 resonated with findings from diverse polysaccharides. The heteropolysaccharide derived from green alga *Enteromorpha prolifera*, which consisted of rhamnose, glucuronic acid, galactose, arabinose and xylose, was shown in a recent study to alleviate HUA in mice by regulating UA transporter expression²⁴. The efficacy divergence between LEP20 and LEP50 suggested that structural distinctions, particularly glycosidic linkage patterns and monosaccharide composition, might influence polysaccharide-target interactions.

LEP20 and LEP50 diminishing hepatic XOD activity and attenuating hepatic injury

UA was primarily synthesized in the liver, where XOD activity was orders of magnitude higher than in other tissues³⁶. Thus, inhibiting hepatic XOD-driven UA production represented a critical strategy for reducing serum UA levels. To further explore the HUA mechanisms of LEP20 and LEP50, we assessed hepatic XOD activity in HUA rats. As shown in Fig. 5A, XOD activity in the MC group was significantly elevated compared to the NC group, confirming that HUA exacerbated hepatic UA synthesis. Administration of LEP20 and LEP50 reduced hepatic XOD levels from 9.34 U/g protein to 6.77 U/g protein and 6.90 U/g protein, corresponding to inhibition rates of 27.56% and 26.18%, respectively. This consistent with established findings that bioactive polysaccharides from diverse natural sources suppress XOD activity, thereby curbing UA overproduction. For instance, both *Ganoderma lucidum* polysaccharide peptide and *Cordyceps militaris* exopolysaccharide reduced serum UA level by inhibiting XOD activity^{37,38}. The efficacy of LEP fractions in modulating XOD activity reinforces their role as multi-target agents for HUA intervention, consistent with their previously demonstrated effects on oxidative-inflammatory axis modulation and UA transporter regulation.

Moreover, chronic HUA is associated with hepatic dysfunction, as evidenced by elevated serum AST and ALT levels³⁹. LEP20 and LEP50 treatments normalized AST and ALT activities in HUA rats (Fig. 5B, C), with LEP20 demonstrating the strongest hepatoprotective effects. Histopathological analysis of hepatic tissues (Fig. 5D) revealed intact hepatic lobules and radially arranged hepatocytes around central veins in the NC group. In contrast, the MC group exhibited disorganized hepatocyte architecture, severe cytoplasmic vacuolization, hepatocellular edema, and inflammatory infiltration in portal areas. LEP20 and LEP50 interventions ameliorated these pathological changes, restoring hepatocyte alignment, reducing vacuolization and edema, and attenuating inflammatory infiltration. In conclusion, LEP fractions mitigated HUA-associated pathology, which was correlated with suppressed hepatic XOD activity and reduced hepatic injury.

LEP20 and LEP50 restoring intestinal barrier integrity and mitigating inflammation

The intestinal microecology encompasses the gut barrier, microbiota, inflammatory status, and metabolic activities⁴⁰. HUA disrupted intestinal barrier function, epithelial integrity, and inflammatory homeostasis. To investigate these effects, we evaluated ileal histopathology, barrier function, and inflammatory cytokine levels in HUA rats. Histological analysis of the ileum (Fig. 6A) revealed uniformly distributed goblet cells with intact mucus vacuoles and smooth muscle layers in the NC group. In contrast, the MC group exhibited villous atrophy, structural fragmentation, disorganized epithelial arrangement, exfoliation of epithelial cells, and dense inflammatory infiltration. LEP20 and LEP50 interventions partially restored ileal architecture, improving villous alignment and reducing inflammatory cell infiltration compared to the MC group.

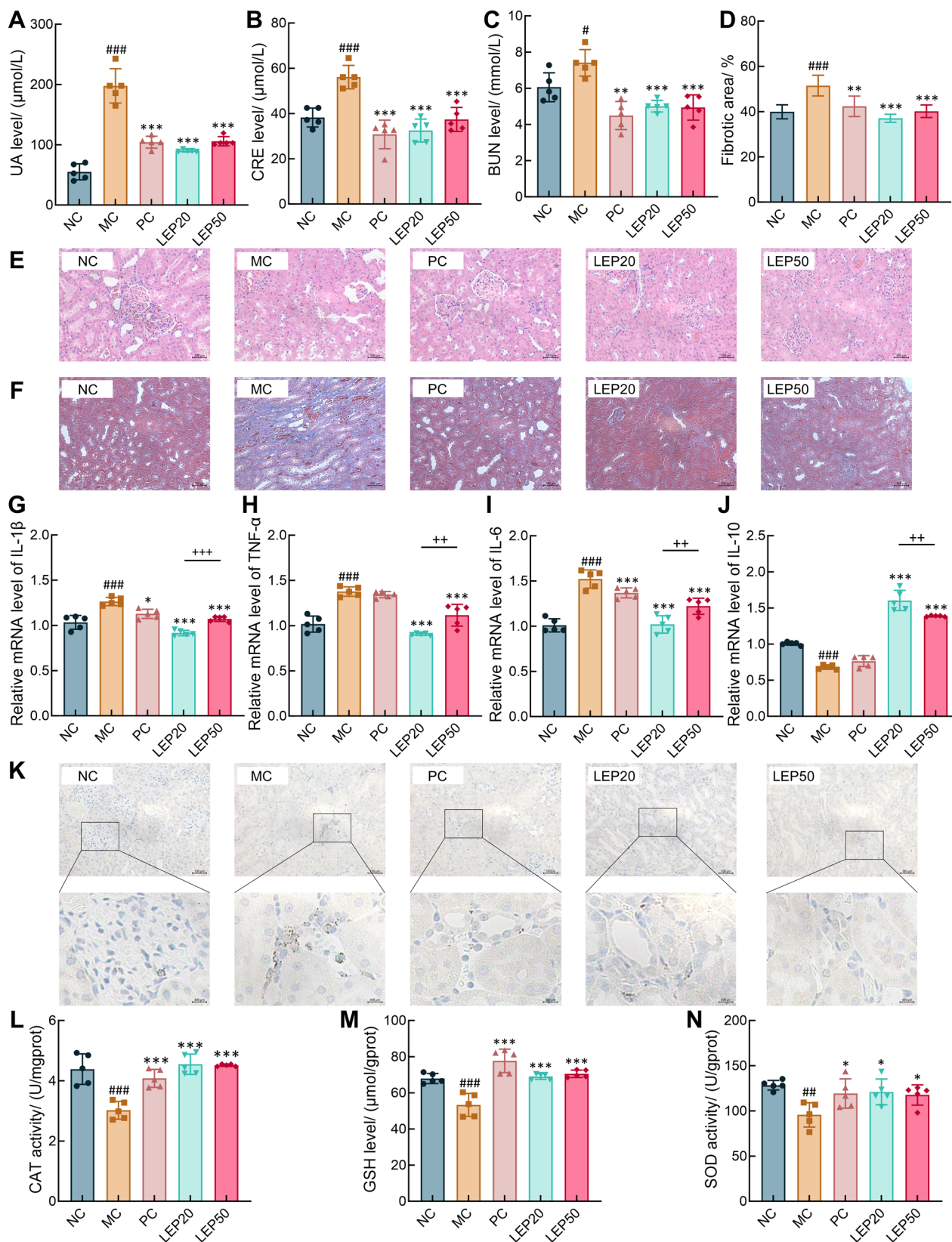


Fig. 3 | Effects of LEP fractions on renal function, inflammation and oxidative stress in HUA rats. The levels of UA (A), BUN (B), and CRE (C) in serum. Renal fibrotic area (D). Micrographs of HE (E) and masson (F) staining kidney (200 ×). The relative mRNA expression levels of IL-1β (G), TNF-α (H), IL-6 (I) and IL-10 (J)

in kidney. IHC staining representative images of CD68 at 200 × (upper row) and 800 × (bottom row) (K). The levels of CAT (L), GSH (M), and SOD (N) in the kidney. **p* < 0.05, ***p* < 0.01 and ****p* < 0.001 vs. NC group; **p* < 0.05, ***p* < 0.01 and ****p* < 0.001 vs. MC group. ++*p* < 0.01 and +++*p* < 0.001 vs. sample groups.

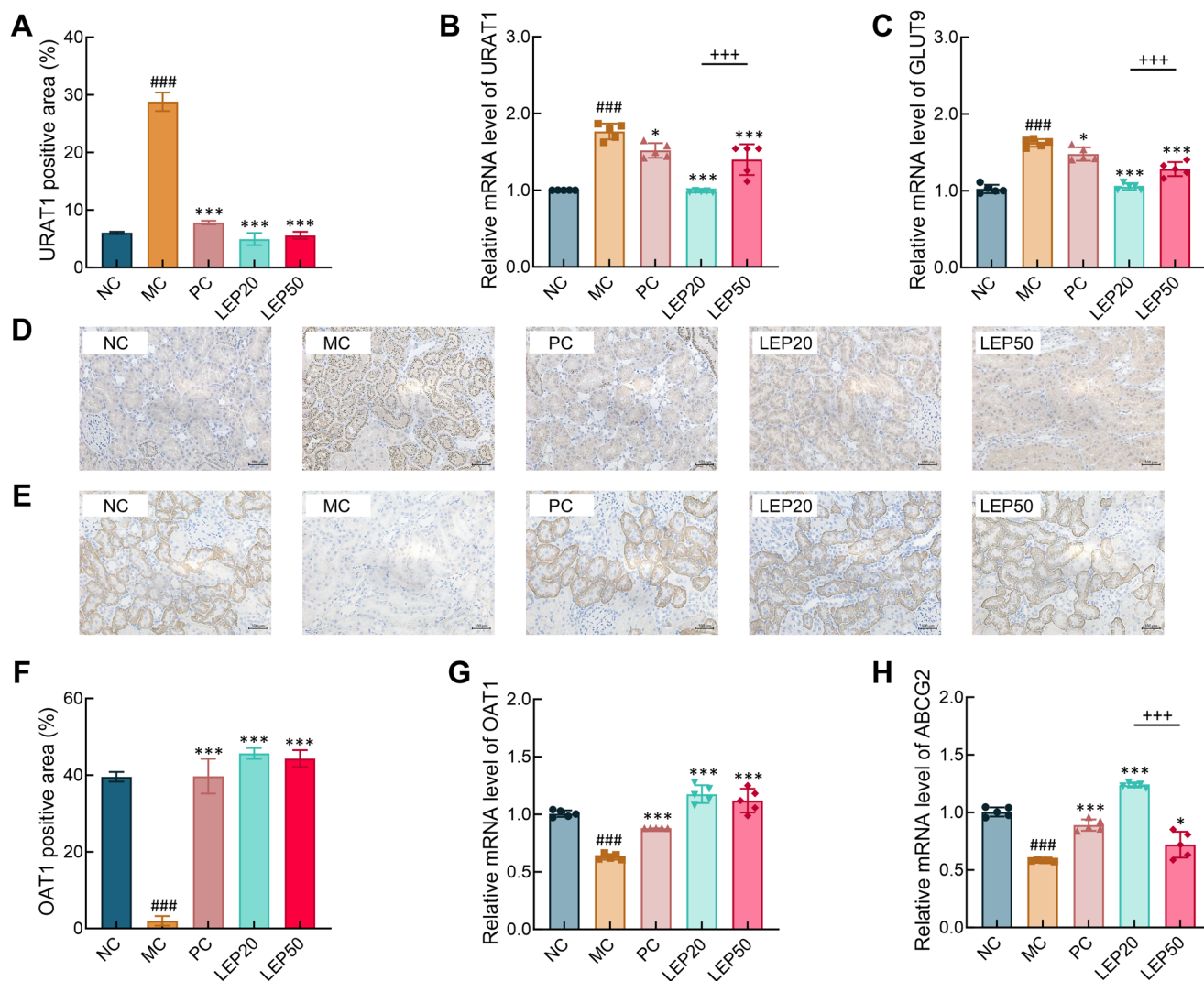


Fig. 4 | Effect of LEP fractions on renal UA transporters in HUA rats. Representative images of IHC staining (200 ×) of URAT1 (D) and OAT1 (E) with their expressions (A, F) in the kidney. The relative mRNA expression levels of URAT1

(B), GLUT9 (C), OAT1 (G), ABCG2 (H) in kidney. ^{***}*p* < 0.001 vs. NC group; ^{*}*p* < 0.05 and ^{***}*p* < 0.001 vs MC group ⁺⁺⁺*p* < 0.001 vs. sample groups.

The mRNA expression levels of tight junction proteins ZO-1, Claudin and Occludin were showed in Fig. 6B–D, which were significantly downregulated in the MC group versus the NC group. LEP treatments attenuated this decline, with LEP20 showing the more pronounced restorative effects on these barrier markers than LEP50, indicating its superior efficacy in mitigating intestinal barrier dysfunction. Pro-inflammatory cytokines IL-1β, IL-6, and TNF-α were markedly upregulated in the ileum of HUA rats (Fig. 6E–G). Both LEP20 and LEP50 suppressed their expression, among which LEP20 comparatively demonstrated the stronger anti-inflammatory activity. As has been noted, LEP20 and LEP50 ameliorated HUA-associated intestinal pathology by restoring tight junction protein expression to reinforce barrier integrity and suppressing pro-inflammatory cytokine production. In particular, LEP20 exhibited superior therapeutic potential, aligning with its enhanced effects observed in renal and hepatic systems. The superior restorative effects of LEP20 on intestinal barrier integrity and anti-inflammatory effect might be consistent with previous findings that β-linked polysaccharides enhanced gut barrier function by suppressing the TLR4-NF-κB signaling pathway and thereby promoting tight junction assembly⁴¹. For instance, yeast β-glucan ameliorate DSS-induced colitis by upregulating expressions of tight junction proteins⁴². In contrast, LEP50 might rely on microbiota-mediated action to indirectly

fortify barrier function, a mechanism observed in *Gastrodia elata* Blume α-glucan that enhanced *Butyricimonas* abundance and inhibited inflammatory response⁴³, resulting in milder efficacy.

LEP20 and LEP50 reshaping gut microbiota composition and function

To elucidate the molecular mechanisms underlying LEP20 and LEP50 interventions in HUA, the gut microbiota composition in rat feces was analyzed using 16S rRNA gene sequencing. Principal component analysis (PCA) revealed distinct clustering of the MC group compared to other groups, indicating that both LEP20 and LEP50 modulated microbial community structure, albeit with divergent taxonomic profiles (Fig. 6H). LefSe analysis identified differentially enriched taxa (LDA score > 4) across groups (Fig. 6I and J). The NC group was characterized by Clostridia, Romboutsia, and Erysipelotrichales, whereas the MC group exhibited enrichment of Lachnospiraceae and Lachnospirales. LEP20-treated rats showed dominance of *Ligilactobacillus*, Lactobacillales, and Bacteroides sp. SB5 (7 taxa), while LEP50 favored Muribaculaceae and Prevotellaceae_UCG_001.

Operational taxonomic unit (OTU) analysis focused on strains with relative abundance > 0.3‰ and significant intergroup differences (*p* < 0.05). Heatmap visualization of 65 differential OTUs (Fig. 7) demonstrated that

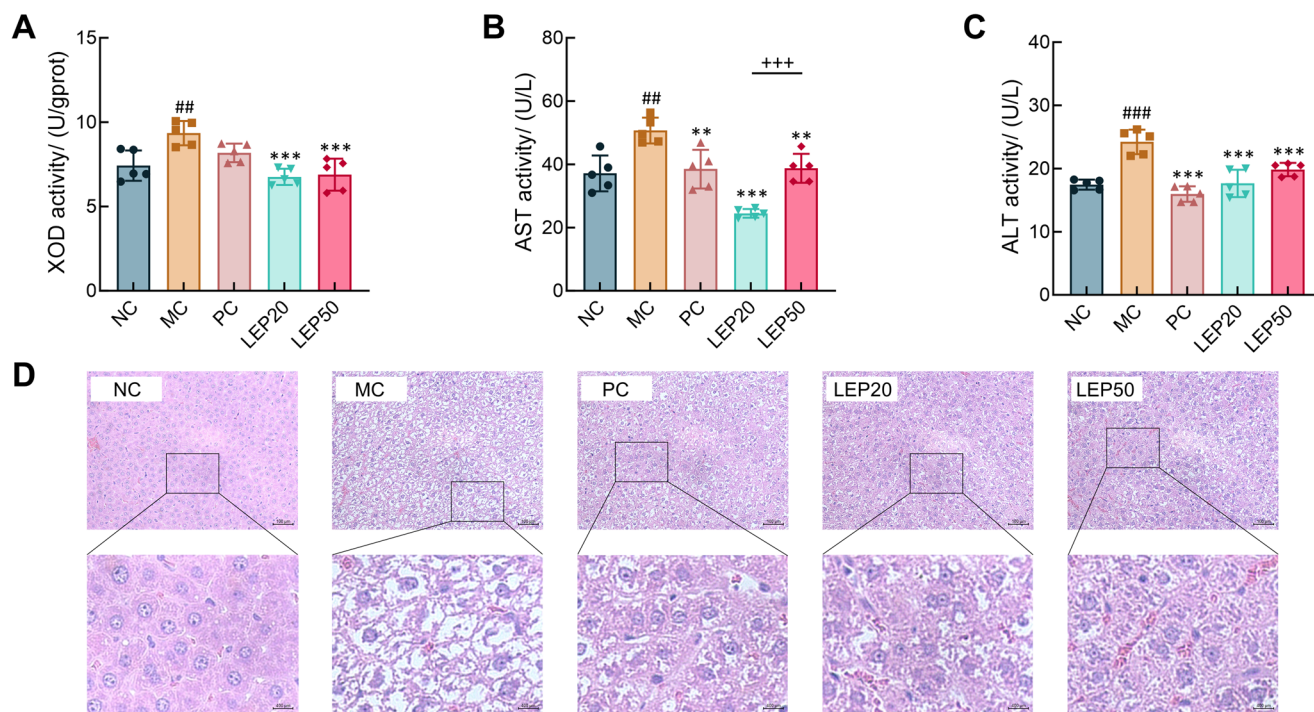


Fig. 5 | Effect of LEP fractions on XOD activity and hepatic injury in HUA rats. The activity of XOD (A) in liver, the activity of AST (B) and ALT (C) in serum. Micrographs of HE staining liver at 200 × (upper row) and 800 × (bottom row)

(D). ** $p < 0.01$ and *** $p < 0.001$ vs. NC group; ** $p < 0.01$ and *** $p < 0.001$ vs MC group; +++ $p < 0.001$ vs. sample groups.

the MC group had 13 OTUs significantly upregulated (e.g., *Frisingicoccus caecimuris*, *Oribacterium*, *Clostridium sp. cTPY_17*, *Dubosiella*, *Bilophila wadsworthia*) and 42 OTUs downregulated (e.g., *Romboutsia ilealis*, *Allobaculum*, *Ligilactobacillus*, *Lactobacillus animalis*) compared to the NC group. LEP20 and LEP50 interventions differentially reversed these dysbiotic patterns. Compared to the MC group, LEP20 and LEP50 altered 19 and 18 OTUs, respectively ($p < 0.05$), with 11 OTUs co-modulated in both groups. Shared upregulated OTUs belonged to Erysipelotrichaceae, Lactobacillaceae, and Muribaculaceae, while abundance of *Clostridium sp. cTPY_17* decreased across both treated groups. Shared modulations, such as increased Lactobacillaceae and decreased *Clostridium sp. cTPY_17*, reflect conserved polysaccharide effects on UA-lowering taxa and inflammation-suppressing pathways^{44,45}. LEP20 specifically elevated 14 OTUs (e.g., *UCG_010*, *Blautia luti*, *Parasutterella excrementihominis*) and reduced 5 OTUs (including 3 Muribaculaceae taxa). *Blautia luti* as a SCFA-producing bacteria, especially butyrate⁴⁶, which elevated SCFAs levels to enhance intestinal barrier integrity. Meanwhile, it suppressed pro-inflammatory Muribaculaceae strains associated with UA retention⁴⁷. In contrast, LEP50 increased 14 OTUs (e.g., *Romboutsia ilealis*, *Frisingicoccus caecimuris*, *Negativibacillus*, *UCG_005*) and suppressed 4 OTUs (*Bilophila wadsworthia*, *Clostridium sp. cTPY_17*, and taxa from Lachnospiraceae and Oscillospiraceae). LEP50 uniquely upregulated *Romboutsia ilealis*, a beneficial bacterium with immunomodulatory effects⁴⁸, and reduced *Bilophila wadsworthia*, a sulfate-reducing pathobiont driving intestinal inflammation⁴⁹. These structural-driven divergences align with previous research showing that different structured polysaccharides have different effects on the gut microbiota⁵⁰, underscoring glycosidic linkage-dependent microbiota interactions. These findings indicated that LEP20 and LEP50 had different remodeling effects on the microbiota, highlighting polysaccharides regulate the microbiota in HUA intervention.

To functionally elucidate the potential microbial contributions to the observed HUA alleviation, PICRUST2 prediction analysis on the KEGG metabolic pathways was performed based on the 16S rRNA gene sequencing data (Figure S1). The results demonstrated that the HUA model induced widespread metabolic disruption, including key nucleotide and amino acid

metabolism, being significantly different from the NC group. Among pathways relevant to purine homeostasis, only LEP50 group showed a significant modulation of the Purine metabolism pathway compared to the MC group, whereas the LEP20 group did not exhibit significant changes in this pathway. This functional prediction supported the observation that LEP50 might drive unique metabolic shifts related to purine precursor turnover within the gut, thereby contributing to the differences observed in the untargeted metabolomics analysis between the two polysaccharide fractions.

LEP20 and LEP50 increasing the level of SCFAs in feces

Short-chain fatty acids (SCFAs) were key metabolites produced by gut microbiota, which played a pivotal role in maintaining intestinal homeostasis. We quantified fecal SCFAs levels in HUA rats, including total SCFAs and individual acids (acetate, propionate, butyrate, isovalerate, and valerate). As shown in Fig. 8A and B, the MC group exhibited significantly reduced total SCFAs and all measured acid concentrations compared to the NC group. LEP20 and LEP50 interventions partially restored SCFAs levels, with LEP20 demonstrating superior efficacy. LEP20 significantly elevated acetate, propionate, and butyrate levels, while LEP50 only increased acetate and propionate. The superior restoration of fecal SCFAs by LEP20, particularly butyrate, a critical modulator of intestinal barrier integrity and NLRP3 inflammasome suppression⁵¹, aligns with its selective enrichment of butyrogenic *Blautia luti*⁴⁶. In contrast, LEP50's limited effect on butyrate reflects its reliance on acetate- and propionate-producing taxa. The ability of LEP20 to elevate butyrate, a potent anti-inflammatory metabolite, further supported its association with attenuated renal inflammation and restored intestinal barrier function compared to LEP50. These observations reinforced that glycosidic linkage patterns appeared to influence polysaccharide-microbiota metabolic interactions. Specially, β -configuration of LEP20 favoring butyrate-centric pathways and the α -linkage of LEP50 engaging broader but weaker metabolic networks. The pronounced metabolic differences are hypothesized to correlate strongly with the resistance of the glycosidic linkage to microbial enzymatic hydrolysis, which is its fermentation kinetics. The β -(1 \rightarrow 3) linkage, especially in its ordered, helical state, exhibited high enzymatic resistance⁵¹.

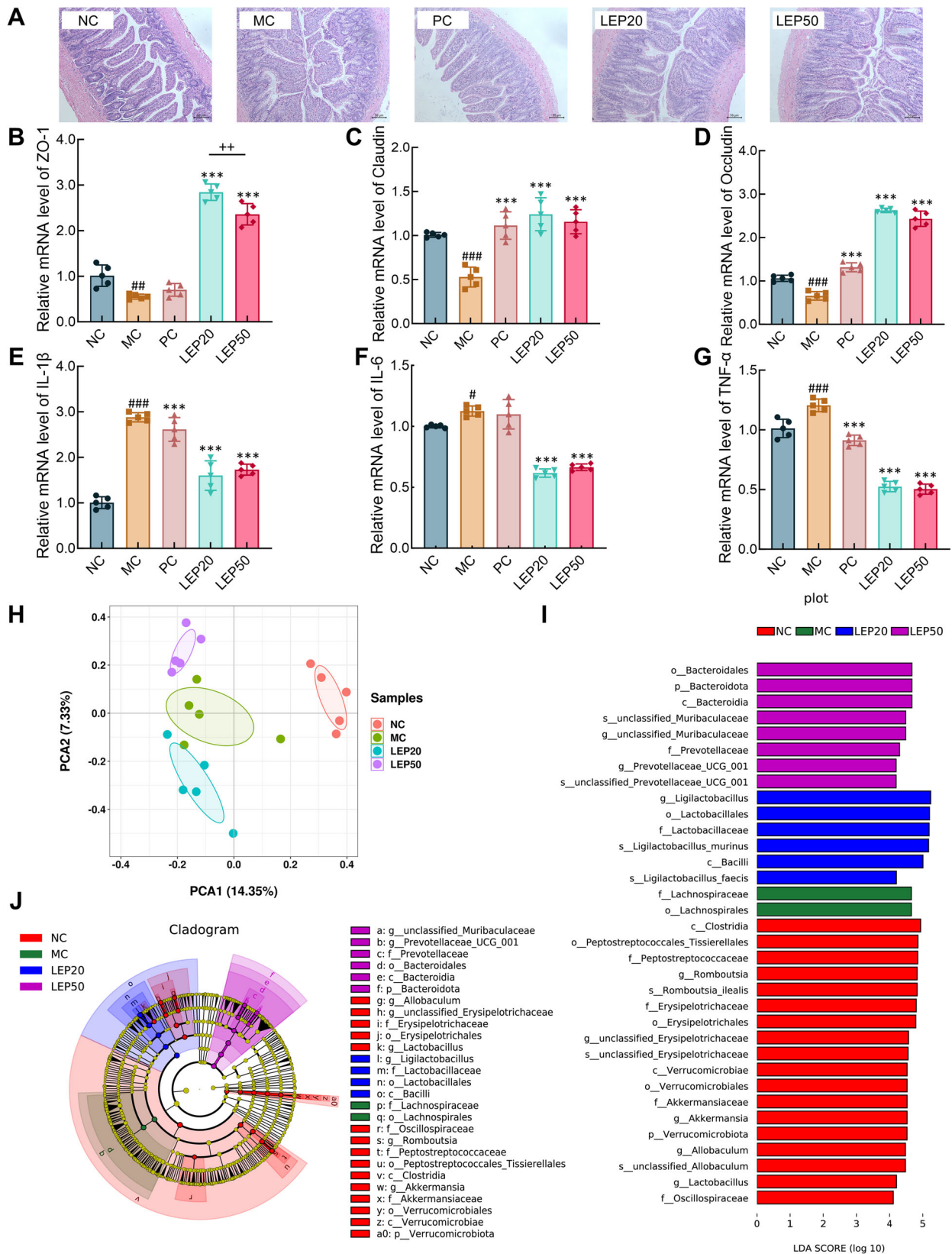


Fig. 6 | Effects of LEP fractions on intestinal mucosal barrier, inflammatory response and microorganism in HUA rats. Micrographs of HE staining ileum (100 ×) (A). The relative mRNA expression levels of ZO-1 (B), Claudin (C), Occludin (D), IL-1β (E), IL-6 (F), TNF-α (G) in ileum. PCA analysis (H), histogram (I) and cladogram (J) generated by LEfSe analysis to show the biomarkers with

statistical difference between different groups at the phylum, class, order, family, and genus levels (LDA score > 4). **p* < 0.05, ***p* < 0.01 and ****p* < 0.001 vs. NC group; ****p* < 0.001 vs. MC group; ++*p* < 0.01 vs. sample groups. PCA and LEfSe analyses were performed using the OmicStudio tools (<https://www.omicstudio.cn/tool>).

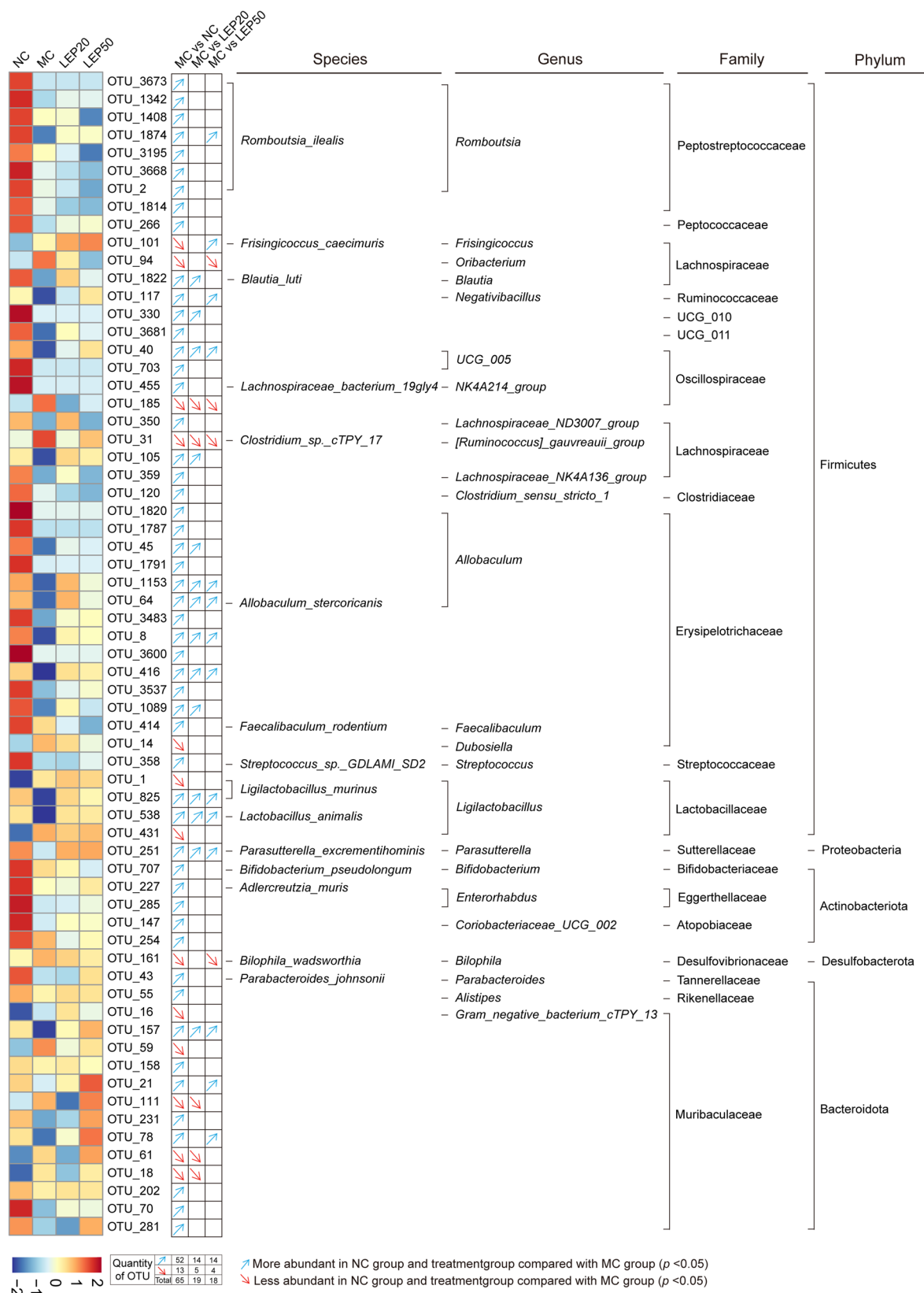


Fig. 7 | Effects of LEP fractions on OTUs of intestinal flora in HUA rats.

LEP20 and LEP50 modulating gut microbiota-derived metabolites linked to UA homeostasis

This study employed LC-MS/MS-based untargeted metabolomics to analyze fecal metabolites in rats from the NC, MC, LEP20 and LEP50 groups⁵²,

aiming to explore the impact of gut microbiota-derived metabolites on HUA. PCA in both positive and negative ion modes (Fig. 8C and D) demonstrated complete separation between the NC and MC groups. The LEP-treated groups (LEP20, LEP50) clustered closer to the NC group,

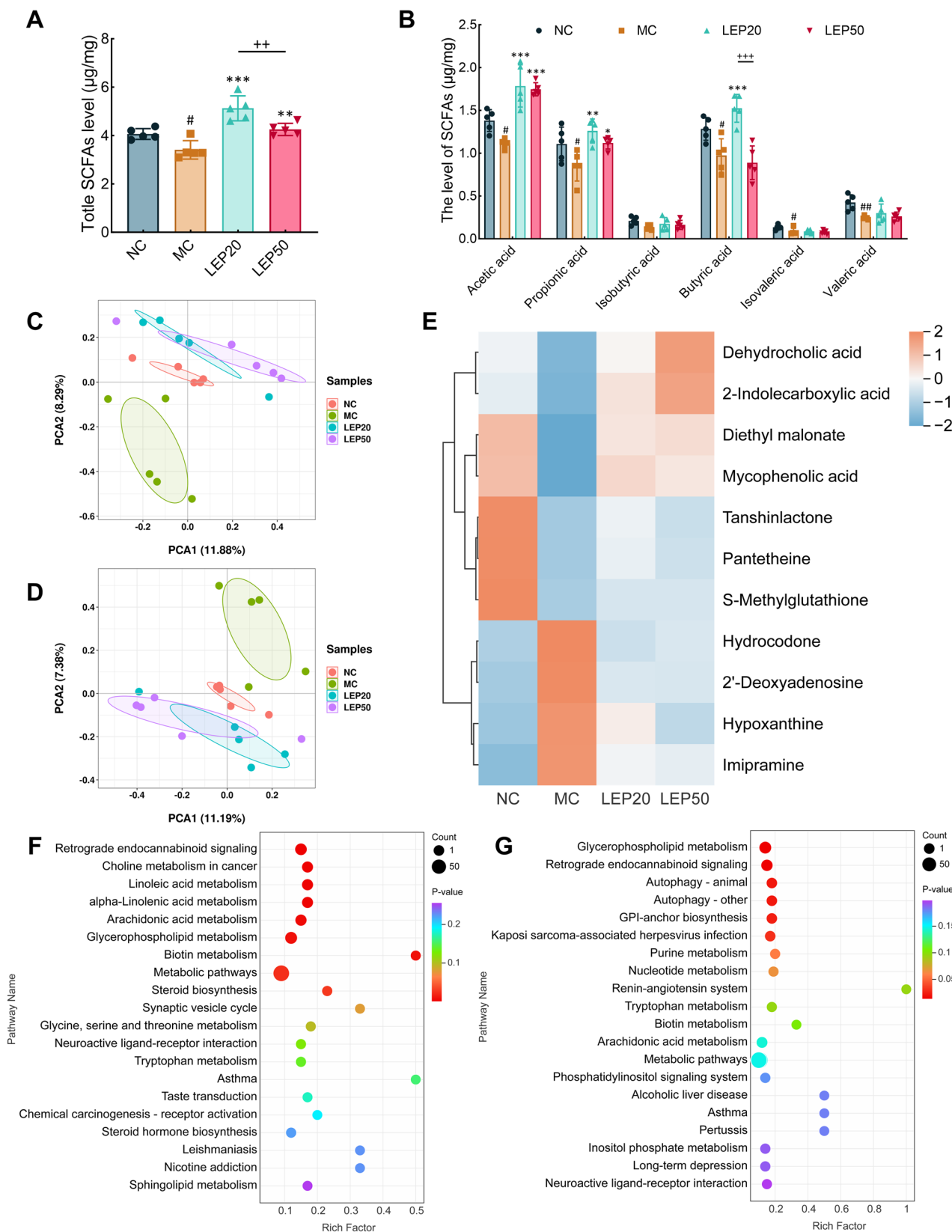
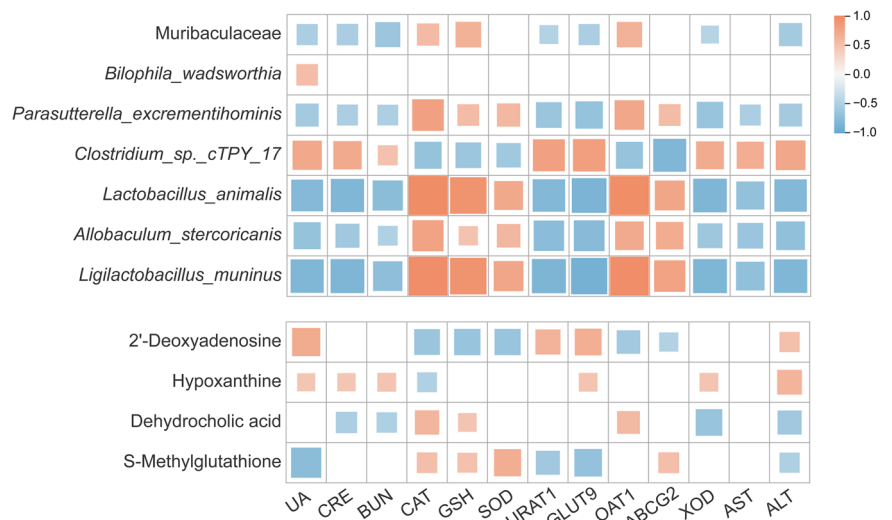


Fig. 8 | Effects of different LEP fractions on fecal metabolites in HUA rats. The levels of total SCFAs (A) and acetic acid, propionic acid, isobutyric acid, butyric acid, isovaleric acid and valeric acid (B) in feces of HUA rats. PCA analysis in positive (C) and negative (D) ion mode. Main differential metabolites among groups (E). Differential metabolic pathway of MC-vs-LEP20 (F) and MC-vs-LEP50 (G). * $p < 0.05$

and ** $p < 0.01$ vs. NC group; * $p < 0.05$, ** $p < 0.01$ and *** $p < 0.001$ vs MC group; + $p < 0.01$ and +++ $p < 0.001$ vs. sample groups. PCA analysis was performed using the OmicStudio tools (<https://www.omicstudio.cn/tool>), and KEGG analysis was performed using the Metware Cloud (<https://cloud.metware.cn>).

Fig. 9 | Correlation heatmap of key gut microbiota, metabolites and HUA-related parameters (Pearson's correlation, $p < 0.05$).



indicating that both polysaccharides modulated fecal metabolite profiles in HUA rats. Differential metabolites were screened using thresholds of fold change (FC) ≥ 2 or ≤ 0.5 , $p < 0.05$, and VIP ≥ 1 . Key metabolites altered by LEP20 and LEP50 were listed in Table S4, and 13 important metabolites were visualized in a heatmap (Fig. 8E). Compared to the MC group, LEP20 upregulated 21 metabolites (e.g., 2-Indolecarboxylic acid, dehydrocholic acid) and downregulated 25 metabolites (e.g., hydrocodone). LEP50 upregulated 27 metabolites (e.g., dehydrocholic acid, diethyl malonate) and downregulated 32 metabolites (e.g., hypoxanthine, hydrocodone). KEGG pathway enrichment analysis further revealed that LEP20 and LEP50 were associated with HUA improvement through different pathways⁵³. LEP20-specific pathways included linoleic acid metabolism, α -linolenic acid metabolism, arachidonic acid metabolism, and tryptophan metabolism (Fig. 8F), while LEP50 uniquely modulated purine metabolism, nucleotide metabolism, tryptophan metabolism, and arachidonic acid metabolism (Fig. 8G). In summary, LEP20 and LEP50 ameliorated HUA concurrently with modulated gut microbiota-associated metabolic pathways, highlighting the potential of LEP as multi-target agents for HUA management through metabolic homeostasis restoration. The untargeted metabolomics revealed different metabolites of LEP20 and LEP50, underscoring how structural specificity may contribute to modulating gut microbiota-host crosstalk. LEP50 elevated dehydrocholic acid, a FXR agonist that enhances bile acid homeostasis and UA excretion⁵⁴, while reducing hypoxanthine, a key XOD substrate⁵⁵. Moreover, although both polysaccharides modulated arachidonic acid and tryptophan metabolism, LEP20 dominated lipid-centric pathways, whereas LEP50 focused on purine and nucleotide metabolism. The findings further revealed that structural specificity likely influenced their divergent interactions.

Correlation analysis of key gut microbiotas and metabolites with HUA-related indicators

Correlation analysis revealed significant associations between HUA-related biochemical indexes and vital gut microbiota and metabolites (Fig. 9). Serum UA levels were positively correlated with 2 pernicious bacteria (*Bilophila_wadsworthia* and *Clostridium sp._cTPY_17*) and 2'-deoxyadenosine and hypoxanthine, which belong to nucleotide and its metabolites. In contrast, Muribaculaceae, *Lactobacillus_animalis* and other beneficial bacteria were negatively related with UA levels, and metabolites S-methylglutathione had the same trend. Renal dysfunction markers CRE and BUN, showed positive correlations with *Clostridium sp._cTPY_17*, implicating this genus might in uremic toxin-mediated renal injury. Antioxidant markers, GSH, CAT and SOD were positively linked to abundances of *Lactobacillus_animalis*, *Ligilactobacillus_muninus* and *Allobaculum_stercoricanis*, and the levels of S-methylglutathione, highlighting their role in

mitigating oxidative stress. Notably, abundance of *Lactobacillus_animalis* and *Ligilactobacillus_muninus* inversely correlated with the AST and ALT levels, suggesting that they also possessed hepatoprotective effects. XOD activity exhibited strong positive correlations with *Clostridium sp._cTPY_17* abundance, suggesting a microbial contribution to purine degradation and urate synthesis. Hypoxanthine, a key purine metabolite, further supported this pathway with its robust correlation to XOD activity. Conversely, abundance of *Lactobacillus_animalis* was inversely associated with URAT1 and GLUT9 expression, and it was positively linked to OAT1 and ABCG2, indicating potential probiotic modulation of urate excretion. Key metabolites also modulated urate dynamics, S-methylglutathione displayed having the same effect as *Lactobacillus_animalis*, resembling pharmacologic uricosurics. Collectively, these findings underscored the gut microbiota-metabolite axis as a critical regulator of systemic urate homeostasis.

Together, the multi-omics evidence indicates that the structural differences between LEP20 and LEP50 shape their distinct regulatory profiles on urate homeostasis (Table S6). The (1 \rightarrow 3)- β -D-glucan LEP20 appears to favor improvements in renal function, antioxidant capacity, and intestinal barrier integrity, partly through enrichment of beneficial bacteria, such as *Lactobacillus_animalis* and *Ligilactobacillus_muninus* and their associated metabolites, which correlate with reduced oxidative stress, lower transaminase levels, and enhance urate excretion pathways. In contrast, the (1 \rightarrow 4)- α -D-glucan LEP50 shows stronger associations with suppression of purine metabolism, consistent with decreased levels of purine-derived metabolites and reduced XOD-linked pathways. Correlation analyses further support the contribution of specific microbial taxa and metabolites to favorable modulation of UA transporters and systemic biochemical markers, whereas harmful taxa parallel elevated UA, CRE, and BUN. These integrated patterns suggest that polysaccharide structural specificity influences gut microbiota-metabolite networks and, consequently, the physiological processes relevant to HUA management, highlighting the potential of structure-guided optimization for future functional applications.

Methods

Materials

The fruit bodies of *L. edodes* (cultivar 'Shenxiang 1513') were supplied by Shiyang Academy of Agricultural Sciences (Hubei, China). Detailed information on all reagents and antibodies used in this study is provided in Supplementary information.

Extraction and purification of polysaccharides from *L. edodes*

The preparation process of the LEP20 and LEP50 was showed in Fig. 1A. The dried powder from *L. edodes* fruit bodies was extracted to get water extract. Following centrifugation (8000 rpm, 20 min), the supernatant was

concentrated. Further to isolate and purify the *L. edodes* polysaccharide based on previous reports and molecular weight distribution characteristics of polysaccharides⁵⁶. For LEP20 isolation, the concentrated extract underwent ethanol precipitation with 20% ethanol (v/v) at 4 °C for 6 h. The resultant pellet was collected through centrifugation under identical parameters, subjected to three washing cycles with 25% ethanol, and lyophilized. The remaining supernatant subsequently received additional ethanol to attain 50% concentration (v/v) for secondary precipitation under equivalent conditions. The 50% ethanol-insoluble fraction underwent parallel processing with 55% ethanol washes prior to freeze-drying, yielding LEP50. The yield of fractions was calculated by the weight of freeze-dried fraction and the powder from *L. edodes* fruit body. Total carbohydrate content was analyzed spectrophotometrically using the phenol-sulfuric acid assay⁵⁷, with glucose as calibration standard.

Homogeneity and molecular weight analysis of LEP20 and LEP50

Molecular characterization of LEP20 and LEP50 was performed through HPSEC-MALLS-RI (Waters E2695 HPLC platform, Waters MALLS/RI detectors) using isocratic elution with 50 mM NaNO₃ (0.05% ProClin 200). Samples (100 µL injection) were analyzed at 0.5 mL/min, with molecular parameters calculated via Astra software (v6.1.1).

Monosaccharide composition analysis of LEP20 and LEP50

Monosaccharide characterization of LEP20 and LEP50 was conducted through acid hydrolysis (2 M TFA, 110 °C/4 h) followed by HPAEC-PAD analysis (Dionex ICS-5000⁺ system, CarboPacTM PA20 column). Monosaccharides (L-Fuc, L-Rha, D-Ara, D-Gal, D-Glc, D-Xyl, D-Man, D-Fru, D-GalA, D-GlcA) were quantified via Chromeleon software using certified standards.

Methylation analysis of LEP20 and LEP50

Methylation of LEP20 and LEP50 were performed as described^{58,59}. Dried samples were methylated with dimethyl sulfoxide (DMSO), NaOH and methyl iodide, followed by extraction, hydrolysis, reduction and acetylation to yield partially methylated alditol acetates (PMAAs). Analysis was conducted by GC-MS (Thermo Fisher, USA) using a DB-5MS column (30 m × 0.25 mm × 0.25 µm) with a temperature gradient from 180 °C to 270 °C at 20 °C/min. Methylation patterns were identified by retention times and mass spectral fragmentation, with molar ratios calculated from normalized peak areas.

Nuclear magnetic resonance (NMR) analysis of LEP20 and LEP50

NMR characterization of LEP fractions was executed on a AVANCE NEO FT-NMR Spectrometer (Bruker, Berlin, Germany). For LEP20, sample (15 mg) was solvated in DMSO-d₆/D₂O (0.6:0.1 mL, v/v). LEP50 (25 mg) underwent deuterium exchange via three freeze-drying cycles in D₂O (0.6 mL). Structural elucidation employed a comprehensive NMR strategy: 1D NMR (¹H-NMR and ¹³C-NMR) combined with 2D NMR (COZY, TOCSY, HSQC, HMBC, NOESY). All NMR experiments were performed at 70 °C.

Animal care and treatment

Male Sprague-Dawley rats (200 ± 20 g) were procured from SLAC Laboratory Animal Co Ltd (Shanghai). All experimental protocols were conducted in compliance with NIH animal care guidelines and received formal approval from the Institutional Animal Care Committee of Shanghai Ruitaimosi Biotech (Ethics Approval No. RM202503(18)).

SD rats (n = 5/group) were acclimated for 7 days and assigned to five groups: non-treated control (NC), model control (MC), positive control (PC; allopurinol 100 mg/kg/day), and LEP20/LEP50 (500 mg/kg/day). HUA models (non-NC groups) received daily oral PO (750 mg/kg) and hypoxanthine (200 mg/kg) for 21 days. At the end of the experimental period, all rats were fasted for 12 h prior to tissue collection. The animals were deeply anesthetized with an intraperitoneal injection of 1% sodium pentobarbital (40 mg/kg body weight). Deep anesthesia was confirmed by

the absence of a pedal withdrawal reflex. After achieving a surgical plane of anesthesia, blood samples were collected via the abdominal aorta. Following blood collection, the rats were immediately euthanized by cervical dislocation while still under deep anesthesia to ensure a humane and rapid end of life. Fecal samples and serum were stored at -80 °C. Liver, kidney, and ileum tissues were frozen (-80 °C) or fixed in 4% paraformaldehyde.

Determination of serum, liver and renal biochemical parameters

The levels of UA, BUN, CRE, AST and ALT in serum, XOD activity in liver tissues and the levels of GSH, CAT and SOD in kidney tissues were determined according to the assay kit instructions.

Histopathology analysis

The fixed liver, kidney, and ileum tissues were embedded in paraffin and sectioned into 4 µm slices. Subsequently all tissues were stained with hematoxylin-eosin (HE) for cellular morphology assessment. The kidney tissues were also stained with masson for collagen visualization. Histopathological evaluation was performed using an Axio Observer3 fluorescence inverted microscope (Zeiss, Oberkochen, Germany) (100 ×, 200 × or 400 ×) to analyze tissue architecture alterations.

RT-qPCR analysis

The mRNA expression levels of tumor necrosis factor-α (TNF-α), interleukin-6 (IL-6), interleukin-10 (IL-10), interleukin-1β (IL-1β), URAT1, GLUT9, OAT1 and ABCG2 in kidney, along with TNF-α, IL-6, IL-1β and Occludin, Claudin and zonula occludens-1 (ZO-1) in ileum tissues were detected by RT-qPCR adopted the previous method¹³. The primers were showed in Table S1 and the relative quantification by 2^{-ΔΔCT} method with β-actin as a control gene.

Immunohistochemistry (IHC) analysis

Kidney tissue sections were incubated with anti-URAT1/OAT1/CD68 primary antibodies (1:200 in PBS, 4 °C/overnight), followed by HRP-conjugated secondary antibodies (1:500, 1 h) and DAB staining. Imaging was performed using a Zeiss Axio Observer3 microscope (200×/400×). Quantitative immunoreactivity analysis was conducted via ImageJ using threshold calibration.

Determination of Short-Chain Fatty Acids (SCFAs) contents in feces

The extraction and testing of SCFAs in feces were performed as below. Homogenize 100 mg feces with 500 µL saturated NaCl solution on ice. Then add 20 µL 10% H₂SO₄ and 500 µL diethyl ether to mix and centrifuge (14,000 rpm, 15 min). Transfer the supernatant to tube with 0.25 g Na₂SO₄, centrifuge again. Transfer final supernatant to GC vial for analysis. Perform GC analysis using conditions described in ref. 59. Quantify using external standard method: Inject mixed standards (acetic, propionic, butyric, isobutyric, valeric, isovaleric acids) to generate calibration curves. The sample concentrations were calculated from regression equations.

Gut microbiota analysis

Fecal DNA was extracted by a Stool DNA Extraction Kit. DNA concentration and quality were measured by a Qubit 4.0 (ThermoFisher, USA). The 16S rRNA gene was amplified by PCR with the primers (F: 5'-AGRGTTYGATYMTGGCTCAG-3' and R: 5'-RGYTACCTTGTTACGACTT-3'). After a series of purification steps, the final sequencing library was obtained. The qualified library was sequenced on the PacBio Revio (Pacific Biosciences, California, USA) for long-read sequencing data. In order to study the species composition of samples, clustered OTU according to the 97% sequence similarity. The β diversity and LEfSe analysis were analyzed based on OTU data.

Untargeted metabolomics analysis

Fecal samples were homogenized in methanol: acetonitrile (1:1, v/v) with 0.1% formic acid. After centrifugation (14000 rpm, 15 min), supernatants

were dried under nitrogen and reconstituted in acetonitrile: water (1:1) for further analysis. LC-MS Conditions refer to the previous methods⁶⁰, and analyses were performed in both positive and negative ion modes. Raw data were processed using ProteoWizard for peak alignment, normalization, and metabolite annotation against integrated public database, AI database and metDNA. The data were analyzed by PCA. Differential metabolites were screened using OPLS-DA, followed by KEGG annotation and pathway enrichment analysis.

Statistical analysis

Statistical analysis was conducted using GraphPad Prism (version 10.1.2). Measurement data were expressed as mean \pm standard error means (SEM), and group comparisons were assessed by one-way ANOVA. A threshold of $p < 0.05$ was defined as statistically significant.

Data availability

The data that support the findings of this study are available from the corresponding author, Yanfang Liu, upon reasonable request.

Received: 31 July 2025; Accepted: 6 January 2026;

Published online: 16 January 2026

References

- Liu, M. et al. Pathophysiological mechanisms of hyperuricemia and the therapeutic potential of food and medicine homologous substances. *Adv. Funct. Foods* **1**, 93–125 (2025).
- Collaborators, G. B. D. G. Global, regional, and national burden of gout, 1990–2020, and projections to 2050: a systematic analysis of the Global Burden of Disease Study 2021. *Lancet Rheumatol.* **6**, e507–e517 (2024).
- Asghari, K. M. et al. Gout: global epidemiology, risk factors, comorbidities and complications: a narrative review. *BMC Musculoskelet. Disord.* **25**, 1047 (2024).
- Sun, Z., Wu, K., Ullah, I. & Zhu, H. Recent advances in xanthine oxidase inhibitors. *Mini-Rev. Med. Chem.* **24**, 1177–1186 (2024).
- Shi, C. et al. Recent advances in gout drugs. *Eur. J. Med Chem.* **245**, 114890 (2023).
- Zhao, Y., Yan, B., Wang, Z., Li, M. & Zhao, W. Natural polysaccharides with immunomodulatory activities. *Mini Rev. Med. Chem.* **20**, 96–106 (2020).
- Yu, W. et al. The role of dietary polysaccharides in uric acid regulation: mechanisms and benefits in managing hyperuricemia. *Trends Food Sci. Technol.* **157**, 104902 (2025).
- Ren, L. et al. Natural polysaccharides in the prevention of hyperuricemia: source, classification, mechanism, application in food industry. *Int J. Biol. Macromol.* **286**, 138421 (2025).
- Yu, Z. et al. Structure, chain conformation and antitumor activity of a novel polysaccharide from *Lentinus edodes*. *Fitoterapia* **81**, 1163–1170 (2010).
- Jayachandran, M., Chen, J., Chung, S. S. M. & Xu, B. A critical review on the impacts of β -glucans on gut microbiota and human health. *J. Nutr. Biochem.* **61**, 101–110 (2018).
- Yasar, A. et al. The branching ratio of enzymatically synthesized α -glucans impacts microbiome and metabolic outcomes of in vitro fecal fermentation. *Carbohydr. Polym.* **335**, 122087 (2024).
- Lysakowska, P., Sobota, A. & Wirkijowska, A. Medicinal mushrooms: Their bioactive components, nutritional value and application in functional food production—A review. *Molecules* **28**, 5393 (2023).
- Xiong, X. et al. Anti-hyperuricemia effects of a polysaccharide–protein complex from *Lentinula edodes* mediated by gut–kidney axis. *Int J. Biol. Macromol.* **293**, 139370 (2025).
- Xu, J. et al. Structural diversity requires individual optimization of ethanol concentration in polysaccharide precipitation. *Int J. Biol. Macromol.* **67**, 205–209 (2014).
- Chen, M. & Wang, J. Polysaccharides from *Exocarpium Citri Grandis*: graded ethanol precipitation, structural characterization, inhibition of α -glucosidase activity, anti-oxidation, and anti-glycation potentials. *Foods* **14**, 791 (2025).
- Wang, L., Zhang, P., Chen, Y., Tian, Y. & Chen, J. Physicochemical characterization and in vitro biological activities of water-extracted polysaccharides fractionated by stepwise ethanol precipitation from *Rosa roxburghii* Tratt fruit. *J. Food Meas. Charact.* **16**, 38–48 (2022).
- Huo, R., Wuhanqimuge, Zhang, M., Sun, M. & Miao, Y. Molecular dynamics modeling of different conformations of β -glucan, molecular docking with dectin-1, and the effects on macrophages. *Int J. Biol. Macromol.* **293**, 139382 (2025).
- Rao, Z., Dong, Y., Zheng, X., Tang, K. & Liu, J. Extraction, purification, bioactivities and prospect of lentinan: a review. *Biocatalysis Agric. Biotechnol.* **37**, 102163 (2021).
- Shi, X. D., Li, O. Y., Yin, J. Y. & Nie, S. P. Structure identification of α -glucans from *Dictyophora echinvolvata* by methylation and 1D/2D NMR spectroscopy. *Food Chem.* **271**, 338–344 (2019).
- Timsans, J., Palomaki, A. & Kauppi, M. Gout and hyperuricemia: a narrative review of their comorbidities and clinical implications. *J. Clin. Med.* **13**, 7616 (2024).
- Yang, S., Liu, H., Fang, X. M., Yan, F. & Zhang, Y. Signaling pathways in uric acid homeostasis and gout: from pathogenesis to therapeutic interventions. *Int. Immunopharmacol.* **132**, 111932 (2024).
- Wang, Z. et al. Effects of *Sporisorium reilianum* polysaccharides and *Phoenix dactylifera* monosaccharides on the gut microbiota and serum metabolism in mice with fructose-induced hyperuricemia. *Arch. Microbiol.* **204**, 436 (2022).
- Wang, X. et al. Screening of uric acid-lowering active components of corn silk polysaccharide and its targeted improvement on renal excretory dysfunction in hyperuricemia mice. *J. Funct. Foods* **86**, 104698 (2021).
- Li, X. et al. The anti-hyperuricemic effects of green alga *Enteromorpha prolifera* polysaccharide via regulation of the uric acid transporters in vivo. *Food Chem. Toxicol.* **158**, 112630 (2021).
- Legentil, L. et al. Molecular interactions of β -(1 \rightarrow 3)-glucans with their receptors. *Molecules* **20**, 9745–9766 (2015).
- Wang, S., Wu, Y., Zuo, Z., Zhao, Y. & Wang, K. The effect of vitamin D supplementation on thyroid autoantibody levels in the treatment of autoimmune thyroiditis: a systematic review and a meta-analysis. *Endocrine* **59**, 499–505 (2018).
- Vonka, V. et al. Kynurenine and uric acid levels in chronic myeloid leukemia patients. *Oncoimmunology* **4**, e992646 (2015).
- Tan, H. et al. Mechanism of macrophages in gout: recent progress and perspective. *Heliyon* **10**, e38288 (2024).
- Guan, F. et al. Tissue macrophages: Origin, heterogeneity, biological functions, diseases and therapeutic targets. *Signal Transduct. Target Ther.* **10**, 93 (2025).
- Roszczyk, A., Turlo, J., Zagodzdzon, R. & Kaleta, B. Immunomodulatory properties of polysaccharides from *Lentinula edodes*. *Int J. Mol. Sci.* **23**, 8980 (2022).
- Du, B., Lin, C., Bian, Z. & Xu, B. An insight into anti-inflammatory effects of fungal β -glucans. *Trends Food Sci. Technol.* **41**, 49–59 (2015).
- Riaz, M. et al. Carvacrol alleviates hyperuricemia-induced oxidative stress and inflammation by modulating the NLRP3/NF- κ B pathway. *Drug Des. Devel Ther.* **16**, 1159–1170 (2022).
- Chen, T. et al. Antioxidant activity of polysaccharides from natural sources. *Acta Pol. Pharm.* **80**, 705–716 (2023).
- Singla, A. et al. β -glucan as a soluble dietary fiber source: origins, biosynthesis, extraction, purification, structural characteristics, bioavailability, biofunctional attributes, industrial utilization, and global trade. *Nutrients* **16**, 900 (2024).
- Adomako, E. A. & Moe, O. W. Uric acid transport, transporters, and their pharmacological targeting. *Acta Physiologica* **238**, e13980 (2023).
- Lou, Y. et al. Ferulic acid ameliorates hyperuricemia by regulating xanthine oxidase. *Int. J. Biol. Macromolecules* **253**, 126542 (2023).

37. Lin, S. et al. *Ganoderma lucidum* polysaccharide peptide alleviates hyperuricemia by regulating adenosine deaminase and urate transporters. *Food Funct.* **13**, 12619–12631 (2022).
38. Ma, L., Zhang, S., Yuan, Y. & Gao, J. Hypouricemic actions of exopolysaccharide produced by *Cordyceps militaris* in potassium oxonate-induced hyperuricemic mice. *Curr. Microbiol.* **69**, 852–857 (2014).
39. Xu, C. et al. Xanthine oxidase in non-alcoholic fatty liver disease and hyperuricemia: one stone hits two birds. *J. Hepatol.* **62**, 1412–1419 (2015).
40. Mostafavi Abdolmaleky, H. & Zhou, J. R. Gut microbiota dysbiosis, oxidative stress, inflammation, and epigenetic alterations in metabolic diseases. *Antioxidants* **13**, 985 (2024).
41. Zhang, X. et al. β -Glucan protects against necrotizing enterocolitis in mice by inhibiting intestinal inflammation, improving the gut barrier, and modulating gut microbiota. *J. Transl. Med.* **21**, 14 (2023).
42. Li, S. et al. Yeast β -glucan attenuates dextran sulfate sodium-induced colitis: involvement of gut microbiota and short-chain fatty acids. *Int. J. Biol. Macromol.* **280**, 135846 (2024).
43. Tan, Y., Cao, W., Yang, L., Gong, X. & Li, H. Structural characterization of the glucan from *Gastrodia elata* Blume and its ameliorative effect on DSS-induced colitis in mice. *Int. J. Biol. Macromol.* **275**, 133718 (2024).
44. Rodriguez, J. M. et al. A randomized pilot trial assessing the reduction of gout episodes in hyperuricemic patients by oral administration of *Ligilactobacillus salivarius* CECT 30632, a strain with the ability to degrade purines. *Front Microbiol.* **14**, 1111652 (2023).
45. Manion, J. et al. *C. difficile* intoxicates neurons and pericytes to drive neurogenic inflammation. *Nature* **622**, 611–618 (2023).
46. Van-Wehle, T. & Vital, M. Investigating the response of the butyrate production potential to major fibers in dietary intervention studies. *NPJ Biofilms Microbiol.* **10**, 63 (2024).
47. Wang, H. et al. Nanoparticles isolated from porcine bone soup ameliorated dextran sulfate sodium-induced colitis and regulated gut microbiota in mice. *Front Nutr.* **9**, 821404 (2022).
48. Song, B. et al. The improvement of immunity and activation of TLR2/NF- κ B signaling pathway by *Romboutsia ilealis* in broilers. *Anim. Sci. J.* **102**, skae286 (2024).
49. Natividad, J. M. et al. *Bilophila wadsworthia* aggravates high fat diet induced metabolic dysfunctions in mice. *Nat. Commun.* **9**, 2802 (2018).
50. Xue, H., Tang, Y., Zha, M., Xie, K. & Tan, J. The structure-function relationships and interaction between polysaccharides and intestinal microbiota: a review. *Int. J. Biol. Macromol.* **291**, 139063 (2025).
51. Caetano-Silva, M. E. et al. Inhibition of inflammatory microglia by dietary fiber and short-chain fatty acids. *Sci. Rep.* **13**, 2819 (2023).
52. Zhao, L. et al. Pivotal interplays between fecal metabolome and gut microbiome reveal functional signatures in cerebral ischemic stroke. *J. Transl. Med.* **20**, 459 (2022).
53. Huckvale, E. D. & Moseley, H. N. B. A cautionary tale about properly vetting datasets used in supervised learning predicting metabolic pathway involvement. *PLoS One* **19**, e0299583 (2024).
54. Qing, Y. et al. Targeted metabolomics reveals aberrant profiles of serum bile acids in patients with schizophrenia. *Schizophrenia (Heidelb.)* **8**, 65 (2022).
55. Fu, Y. et al. *Lactobacillus rhamnosus* GG ameliorates hyperuricemia in a novel model. *npj Biofilms Microbiol.* **10**, 25 (2024).
56. Liu, Y. et al. Physicochemical characterization of a high molecular weight bioactive β -D-glucan from the fruiting bodies of *Ganoderma lucidum*. *Carbohydr. Polym.* **101**, 968–974 (2014).
57. DuBois, M., Gilles, K. A., Hamilton, J. K., Rebers, P. A. & Smith, F. Colorimetric method for determination of sugars and related substances. *Anal. Chem.* **28**, 350–356 (1956).
58. Liu, Y. et al. Structural characterization of a bioactive water-soluble heteropolysaccharide from *Nostoc sphaeroides kutz.* *Carbohydr. Polym.* **200**, 552–559 (2018).
59. Chen, S. et al. Preparation, structural characterization, and in vitro modulation of the gut microbiota activity of a novel α -glucan in *Hericium erinaceus*. *J. Agric Food Chem.* **73**, 8338–8351 (2025).
60. Liang, L. et al. Metabolic dynamics and prediction of gestational age and time to delivery in pregnant women. *Cell* **181**, 1680–1692 (2020).

Acknowledgements

This work was supported financially by Shanghai Agriculture Applied Technology Development Program, China (Grant No. T2023109), the Earmarked Fund for China Agriculture Research System, China (Grant No. CARS-20) and Shanghai Academy of Agricultural Sciences (SAAS) Program for Excellent Research Team (Grant No. G2022003).

Author contributions

X.X. wrote the original draft, developed the methodology, curated the data, and conducted formal analysis; P.L. conceptualized the study and validated the findings; L.L. provided resources; J.F. created visualizations; J.Z. administered the project; J.W. and J.G. performed investigation and developed methodology; Y.L. conceptualized the study, secured funding, supervised the research, reviewed and edited the manuscript. All authors have read and agreed to the published version of the manuscript.

Competing interests

The authors declare no competing interests.

Additional information

Supplementary information The online version contains supplementary material available at <https://doi.org/10.1038/s41538-026-00714-w>.

Correspondence and requests for materials should be addressed to Yanfang Liu.

Reprints and permissions information is available at <http://www.nature.com/reprints>

Publisher's note Springer Nature remains neutral with regard to jurisdictional claims in published maps and institutional affiliations.

Open Access This article is licensed under a Creative Commons Attribution 4.0 International License, which permits use, sharing, adaptation, distribution and reproduction in any medium or format, as long as you give appropriate credit to the original author(s) and the source, provide a link to the Creative Commons licence, and indicate if changes were made. The images or other third party material in this article are included in the article's Creative Commons licence, unless indicated otherwise in a credit line to the material. If material is not included in the article's Creative Commons licence and your intended use is not permitted by statutory regulation or exceeds the permitted use, you will need to obtain permission directly from the copyright holder. To view a copy of this licence, visit <http://creativecommons.org/licenses/by/4.0/>.

© The Author(s) 2026